First observation of isolated nuclear recoils following neutron capture for dark matter calibration

A. N. Villano,[1,*] M. Fritts,[2] N. Mast,[2] S. Brown,[1] P. Cushman,[2] K. Harris,[1] and V. Mandic[2]

[1]Department of Physics, University of Colorado Denver, Denver, Colorado 80217, USA
[2]School of Physics and Astronomy, University of Minnesota, Minneapolis, Minnesota 55455, USA

(Received 3 October 2021; accepted 11 April 2022; published 26 April 2022)

Low-energy nuclear recoils (NRs) are hard to measure, because they produce few e^-/h^+ pairs in solids—i.e., they have low "ionization yield." A silicon detector was exposed to thermal neutrons over 2.5 live days, probing NRs down to 450 eV. The observation of a neutron capture-induced component of NRs at low energies is supported by the much-improved fit upon inclusion of a capture NR model. This result shows that thermal neutron calibration of very low recoil energy NRs is promising for dark matter searches, coherent neutrino experiments, and improving understanding of ionization dynamics in solids.

DOI: 10.1103/PhysRevD.105.083014

I. INTRODUCTION

The observation of 100-eV-scale nuclear recoils (NRs) is a decades-long detector challenge that is only recently becoming accessible due to new technological advances [1–6]. While the theoretical framework remains deeply rooted in work from the 1960s [7–14], a better and more modern understanding of these low-energy recoils is crucial for progress in several contemporary fundamental physics fields, including dark matter (DM) direct detection and coherent elastic neutrino-nucleus scattering (CEνNS). We have observed isolated NRs in this energy region generated by the neutron capture process in silicon. These NRs are not contaminated by energy deposited by the outgoing gammas from the capture process, and their recoil energies are near threshold for even the most sensitive modern detectors. This technique has been recently suggested [15], but we believe this is the first observation of this kind, enabling more detailed characterization studies of low-energy NRs.

The ultimate goal for this type of measurement is to use the exiting gammas for a coincidence tag to make a high-precision measurement. We have not used this tagging in the present work but have shown that even without the tagging the technique can be used to assess the NR detector response—including *in situ* with low-background experiments. The present measurement has key differences from previous measurements that utilize the capture processes [16,17]. Those previous measurements of the neutron capture allowed experimenters to observe an NR *summed together with* 68 keV of electron-recoil (ER) energy—these energy random variables may be correlated so that their statistics are different when in each others' presence. In any case, the NR energy is less than 1% of the total, and relatively small fluctuations in the ER signal can have a large impact.

II. EXPERIMENTAL CONFIGURATION

NRs were detected in a silicon detector operated at cryogenic temperatures, specifically a prototype SuperCDMS SNOLAB HV detector [18] read out with the superconducting quantum interference devices and cold hardware [19] from CDMS-II Soudan but modified to account for the lower normal-state resistance of the new SuperCDMS SNOLAB HV transition-edge sensors (TESs) [20]. The detector has a diameter of 100 mm and a thickness of 33 mm. Each side has six phonon channels, and each channel of the detector uses parallel arrays of TESs to sense the phonon signal in the silicon substrate. The detector was mounted inside an Oxford Instruments Kelvinox 100 dilution refrigerator [21] at the University of Minnesota and cooled to ∼30 mK. It was operated in the "CDMSlite" mode developed by the SuperCDMS Collaboration [22]. A bias of −125 V was used, and six phonon channels on one side were read out by prototype SuperCDMS detector control and readout boards at a 1.25 MHz sampling rate [23].

The detector, when operated at high bias voltage, takes advantage of the Neganov-Trofimov-Luke (NTL) effect for phonon amplification [24,25], in which the phonon energy E_t produced from a recoil of energy E_r is dominated by secondary NTL phonons:

$$E_t = E_r\left(1 + Y(E_r)\frac{\mathrm{eV}}{\varepsilon_\gamma}\right), \tag{1}$$

*Corresponding author.
anthony.villano@ucdenver.edu

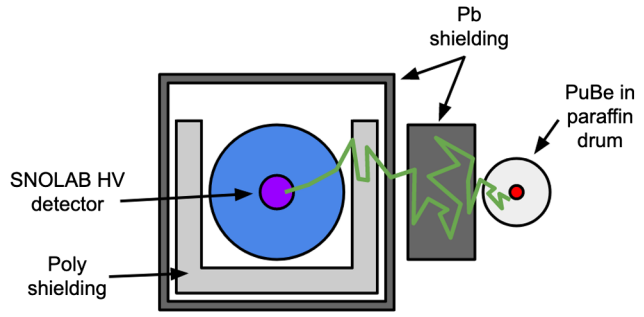

FIG. 1. Top-down view of experimental setup. Cartoon of thermalizing neutron shown in green.

where V is the bias voltage and ε_γ is the average ER energy required to produce an e/h pair (3.8 eV in Si [26]). $Y(E_r)$ is a dimensionless quantity known as the ionization yield and is normalized to unity for the mean ER response. The ionization from a NR is less than half of that from an ER and varies with recoil energy. Our detector calibrations are based on an ER source, so we refer to this energy scale as "electron equivalent" and denote it by $\mathrm{eV_{ee}}$. The ionization yield determines how NRs appear on this energy scale. Figure 1 shows the experimental setup. Neutrons were produced by a PuBe source (1.4 Ciα, 62 μCi n) enclosed in a paraffin-filled drum to reduce their energy. The alpha and neutron rates are calculated based on the original source documentation, taking into account changes over time from the decay of ^{241}Pu to ^{241}Am. See Fig. 2 for the distribution of neutrons and gammas coming from the source. The cryostat was shielded on three sides and below by 20.3 cm of polyethylene for further neutron moderation. It was also surrounded on four sides by 1.6-cm-thick lead to reduce gamma backgrounds. Finally, a 30.5 cm lead wall was constructed to block direct ~MeV gammas from the PuBe source. The wall was placed near the PuBe drum in the line of sight to the SuperCDMS detector. A 1 μCi ^{241}Am calibration source was mounted in the detector housing. The source encapsulation effectively blocked gamma emission at energies below 5 keV. A 1.6-mm-thick lead disk with a 0.5-mm-diameter hole collimated the source gammas and restricted the emission rate to less than 25 Hz. A strip of Kapton tape placed over the collimator blocked alpha emission.

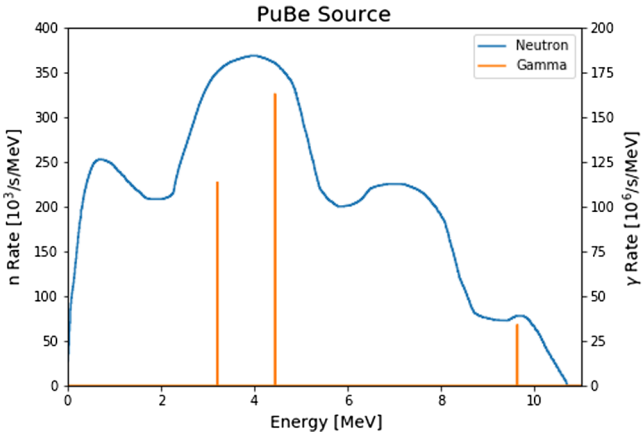

FIG. 2. PuBe source spectrum. The neutrons from the source were measured in the early reference [27], and the gammas come from the accompanying deexcitation of the residual ^{12}C system. The neutrons are emitted in broad groups corresponding to the excitation level of the residual system and the amount of stopping experience by the α prior to the (α, n) reaction.

A. Triggering

A simple trigger quantity was defined as the difference between the average sample value in two consecutive windows, the first 12.8 μs wide and the second 4 μs wide. If trigger thresholds were exceeded on any one of three phonon channels, a 3.2768 ms trace was recorded. The trigger threshold values were set as low as possible while keeping the rate of noise triggers below 150 Hz.

Three datasets were taken for this study: one signal dataset with the PuBe source in place; a background dataset with no external source; and a calibration dataset with a strong ^{22}Na source outside the cryostat. The total live time for the PuBe dataset after cuts (see Sec. III) was approximately 2.5 live days.

III. DATA ANALYSIS

Phonon pulse amplitudes were extracted from raw traces using the optimal filter (OF) algorithm (Appendix B of Ref. [28]), which fits a pulse template to the measured trace by minimizing the frequency domain χ^2 weighted by the measured noise spectrum. The algorithm returns the best-fit amplitude and start time. To decrease computational time, the start time is required to fall within a 100 μs window around the trigger time.

A. Energy calibration

Energy calibration for ERs was performed using several low-energy x-ray lines associated with the ^{241}Am source shown in Fig. 3. The analysis range for our PuBe dataset is 50 $\mathrm{eV_{ee}}$ to 2 $\mathrm{keV_{ee}}$. The ER scale was calibrated separately for each dataset using two prominent x-ray lines from ^{241}Am: 14.0 and 17.7 keV. The data were fitted by assuming that the OF zero corresponded to zero energy and employed a quadratic fit. Fits were nearly linear with a small quadratic correction, accounting for TES saturation. This fit showed good agreement with the other five identified lines below 20 keV down to our lowest line at 8 keV (copper fluorescence line that we can barely identify). The other identified fluorescence lines make sense, because our Am source was removed from a smoke detector where Pb, Au, and Ag are used in the construction [29]. The lines came from Pb (10.5 and

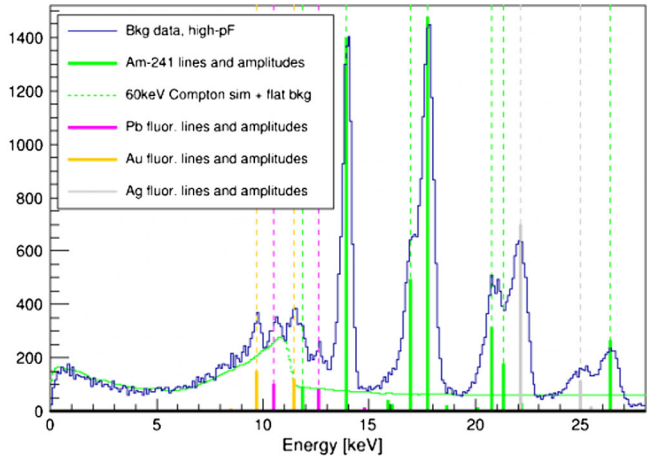

FIG. 3. Calibration lines in the background energy spectrum with selection of events near the Am-241 calibration source.

12.5 keV), Au (9.6 and 11.5 keV), and Ag (two above 20 keV). These lines are identified in Fig. 3.

The energy resolution in $\mathrm{eV_{ee}}$ was modeled as $\sigma_{\mathrm{ee}}^2 = \sigma_0^2 + (B + \varepsilon_\gamma F)E_{\mathrm{ee}}$ and was fit using all the following lines: 9.6, 10.5, 12.5, 14.0, 17.7, and 22.1 keV. A point at 0 keV was included by using the width of randomly triggered noise event fits. The parameter σ_0 is the baseline resolution, $F = 0.1161$ is the ER Fano factor [30,31] (known to be different for NRs), and B incorporates any additional energy-dependent resolution effects intrinsic to the detector. The widths of calibration lines and the baseline trace width determine the best-fit values of $\sigma_0 = 10 \pm 5$ $\mathrm{eV_{ee}}$ and $B = 1.9 \pm 0.1$ $\mathrm{eV_{ee}}$, with a χ^2 of 20.7 for 5 degrees of freedom. For ERs, detector and electronic effects have a stronger impact on resolution than the Fano factor.

The low-energy ER calibration is of fundamental importance to our measurement, because the NR ionization is measured relative to it. We believe our calibration procedure—outlined above—produces accurate ER energy measurements down to 50 $\mathrm{eV_{ee}}$. Our nearly linear quadratic fit outlined above for the OF energy tracks the integral of our phonon pulses linearly to our analysis threshold even though it was directly compared only to a known line at 8 keV. That means there is no inherent bias in the OF above our analysis threshold. Furthermore, our assumption of the OF zero corresponding to "zero energy" must be approximately valid, because bias in the OF amplitude is negligible compared to our trigger threshold (around 7 $\mathrm{eV_{ee}}$) and contributes even less at our analysis threshold (around 50 $\mathrm{eV_{ee}}$). Between the zero point and our 8 keV verification, the only plausible possibility is a monotonic calibration function; our nearly linear function fits all known evidence. When applying this procedure to a germanium detector of similar design and operated at a similar voltage, a good fit is obtained down to at least 100 $\mathrm{eV_{ee}}$ with direct verification from a ^{71}Ge electron capture line.

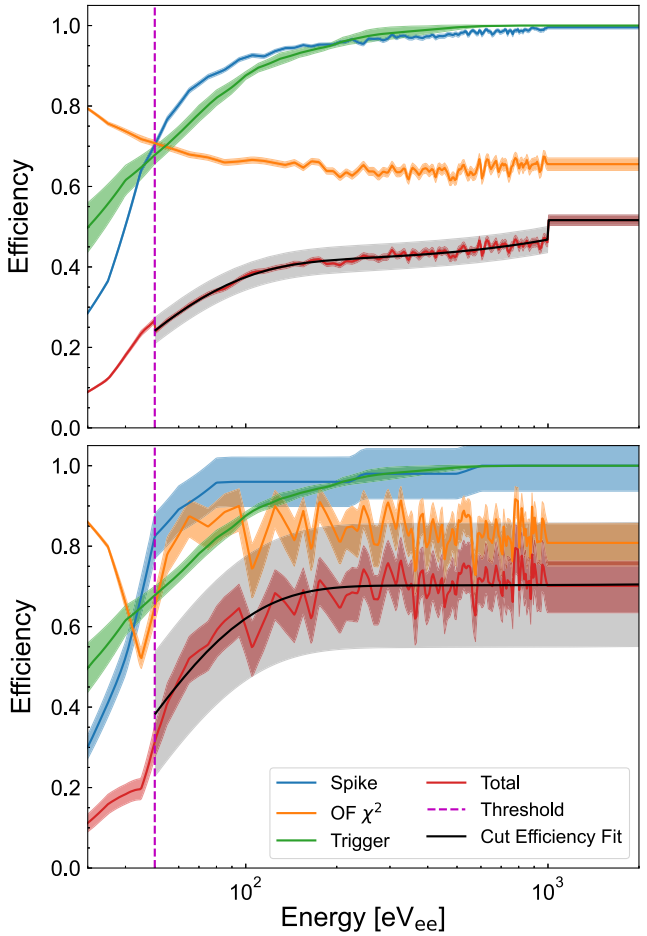

FIG. 4. Energy-dependent efficiencies for PuBe (upper) and background (lower) datasets. Black curves show smooth functional forms of the total cut efficiency used for further analysis.

B. Data quality cuts and efficiencies

The following quality cuts were applied to both background and PuBe data. The cut efficiency was defined as the good event fraction at a given energy that survive the cut. The cut efficiency is shown in Fig. 4 for background and neutron datasets. Further details on these cuts have been given by Mast [32].

1. Baseline cut

Events were removed if the prepulse baseline average or variance was excessively high. This removed events on the tail of an earlier pulse, as well as noisy data. The efficiency was calculated from the passage fraction of randomly triggered traces and was found to be 0.820 ± 0.001 (energy independent).

2. Pileup cut

Events containing multiple pulses were removed based on any of three criteria: (i) the ratio between the integral of the trace (which includes all pulses present) and the fitted

OF amplitude (which fits a single pulse by definition) was larger by 3σ than the median value; (ii) the OF delay was within 1 μs of the early edge or 2 μs of the late edge of the 100-μs-wide fitting window; and (iii) the OF delay was more than 70 μs earlier or more than 10 μs later than the 50% point on the rising edge computed using a pulse-shape characterization algorithm [33]. The passage fraction of the pileup cut was 0.965 ± 0.001, which we used as the energy-independent efficiency for the cut.

3. Spike cut

Events with unusual pulse shapes were occasionally observed but easily removed due to unnaturally fast fall times. The efficiency was energy dependent and is shown in Fig. 4. It was calculated as the passage fraction for datasets in run periods that were mostly free of such events.

4. OF χ^2 cut

The goodness of the OF fit is quantified with a χ^2 calculated in frequency space and weighted by the average noise power spectral density. An energy-dependent cut was defined to remove events with χ^2 per degree of freedom values that exceeded 1.25. Events removed by this cut were mostly ordinary pulses. As such, we assumed the passage fraction of this cut to be its energy-dependent efficiency, shown in Fig. 4.

5. Low-energy trigger burst cut

Short bursts of events below 150 eV_{ee} were occasionally observed. The bursts comprised high-rate (above 1 kHz) periods of otherwise good pulses in the space of tens to hundreds of milliseconds. Bursts were almost nonexistent in background data but significant in the two high-rate datasets. To identify events in bursts, we examined the proximity between consecutive low-energy (below 1 keV) events in the event sequence. Low-energy events were required to be sequentially separated by greater than 20 events. After applying this criterion, the resulting event sequence was consistent with a random distribution of low-energy events. The background dataset was consistent with having no burst events, so this cut was not applied to it.

The cut removed only events between the 50 eV_{ee} analysis threshold and 1 keV_{ee}, where the resulting efficiency was 0.893 ± 0.001 and the estimated leakage fraction was less than two-tenths of a percent. Outside of 50–1000 eV_{ee}, the efficiency was 1.

6. Trigger

The data acquisition system (DAQ) system trigger efficiency was calculated using a distribution of simulated pulses constructed from higher-energy events where the trigger efficiency was 100%, then scaled down to simulate lower-energy events, and added to noise from randomly triggered traces. The trigger algorithm was applied to this distribution to generate an efficiency curve as a function of energy as shown in Fig. 4.

The DAQ has a limited speed, such that some events which trigger are not written. The write efficiency is energy independent but rate dependent. A write efficiency of 0.617 ± 0.004 and 0.815 ± 0.004 for the PuBe and background data, respectively, was measured by comparing the rate of pulses that should pass the trigger to the actual write rate.

IV. CAPTURE SPECTRUM

When a nucleus relaxes after neutron capture, it passes through a number of nuclear levels, emitting as many gammas as levels visited. This deexcitation process is called a cascade, and typically it happens fast enough that all the dynamics appear in one measured event. The properties of the resulting NR depend on the specific cascade realized in that event. Since this is the signal we are attempting to extract from the neutron data, we carefully simulated the cascade event and understand the resulting NR spectrum.

The energy deposits were modeled for individual cascades and then combined with the correct probabilities to make the total spectrum [34]. Each probability is derived from both the relative abundance [35] of the isotope and its capture cross section [36]. The probabilities for each cascade are inferred from the literature [37].

Modeling is simple for one-step cascades. For multistep cascades, several parameters become important, including the stopping properties of recoils, the half-lives of individual energy levels, and the angular distribution of emitted gammas. For stopping properties, we used constant-acceleration stopping equal to the average of the Lindhard stopping power [7]. Half-lives of intermediate levels were taken from measurements where possible; otherwise, Weisskopf estimates were used [38]. The angular distribution of emitted gammas was taken as isotropic. For multistep cascades, the deposited energy is not always a single value like it is for one-step cascades. Depending on the level parameters, multistep cascades can give single values or broad spectra (if there is a decay in flight for the recoil atom).

Silicon has more than 80 such cascades, and many have low probability. While we did model all the cascades, we included only the six most common cascades for ^{29}Si (capture on ^{28}Si), since they provided 94% of the total spectrum for that isotope and adding in all the cascades did not result in a significant change in the shape of the curve. A similar strategy applied to the other isotopes of silicon led to the selection of the four most common cascades for ^{30}Si and ^{31}Si for a total of 14 cascades used. We assumed natural abundances of isotopes. Table I shows the parameters of all the cascades included in our modeling. The expected distributions of the ionization energies due to

TABLE I. A table displaying the cumulative fractional contribution of each cascade identifier (CID) for both the Lindhard and Sorensen models. This table includes only the cascades used. The statistics reported include only events which were above the detector threshold. The isotope listed is the isotope on which the neutron captures; the energy levels and half-lives are therefore for an isotope of silicon with one more neutron. A half-life entry of w(E1) specifies that the half-life is unknown and the Weisskopf estimate for an electric dipole transition was used [38].

Cascade ID (CID)	Isotope	Prob. (%)	Energy levels (keV)	Half-lives (fs)	Cumulative contribution (%) (Lind./Sor.)
1	^{28}Si	62.6	4934.39	0.84	63.6/63.7
2	^{28}Si	10.7	6380.58, 4840.34	0.36, 3.5	75.0/74.0
3	^{28}Si	6.8	1273.37	291.0	83.3/83.4
4	^{28}Si	4.0	6380.58	0.36	88.1/88.7
5	^{28}Si	3.9	4934.39, 1273.37	0.84, 291.0	91.7/91.9
6	^{28}Si	2.1	⋯	⋯	94.3/94.8
7	^{29}Si	1.5	6744.1.0	14	96.1/96.7
8	^{30}Si	1.4	3532.9, 752.2.0	6.9, 530	97.1/97.3
9	^{29}Si	1.2	7507.8, 2235.3.0	24, 215	98.5/98.5
10	^{29}Si	0.4	8163.2.0	w(E1)	99.0/99.1
11	^{30}Si	0.4	5281.4, 752.2.0	w(E1), 530	99.3/99.3
12	^{29}Si	0.3	⋯	⋯	99.7/99.8
13	^{30}Si	0.3	4382.4, 752.2.0	w(E1), 530	100./100.
14	^{30}Si	0.0	⋯	⋯	100./100.

these capture events are shown in Fig. 5 for two probability density functions.

Our model accounted for how often the gammas from capture exited the detector without depositing energy, leaving only the isolated NR behind. This selection did not distort the spectral shape much, cutting out roughly 10% of all the events. These models were used to simulate 10^6 capture cascades for comparison to the observed data (see Sec. VI).

V. NONCAPTURE SPECTRA

An ideal neutron source would produce only thermal neutrons, but a PuBe source also produces gamma radiation and higher-energy neutrons which reach the detector and produce elastic recoils, some of which deposit energies in the analysis region. For a full analysis, it was necessary to model these other components of the observed spectrum.

For these noncapture events (ERs and noncapture NRs), we directly used the deposited recoil energies from ER and NR hits as modeled in GEANT4 [39,40]. We used the version GEANT4.10.1.p02. A complete model of the laboratory configuration was used, including the PuBe source and housing, all shielding elements, the refrigerator frame and main refrigerator components, the main components of the hardware supporting the detector, and the floor, ceiling, and walls, with the intent to fully account for complex neutron paths. We base our PuBe simulated source spectra on Ref. [27].

In the GEANT4 simulation, high-precision electromagnetic physics and neutron physics were used [41,42]. Although newer models of GEANT4 (after GEANT4.10.5) use an upgraded coherent γ-nucleus scattering [43], our simulation uses the older evaluated Photon data library (EPDL) model [44]. The EPDL model has significantly

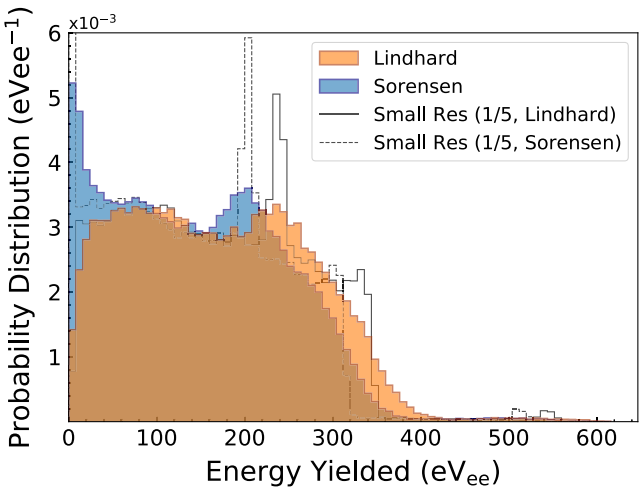

FIG. 5. Overlaid histograms comparing the yielded energy PDFs for Sorensen [11] and Lindhard [7] models, including the resolution of the current detector. The histograms are comprised of approximately 10^6 simulated cascades. The orange (front) filled histogram represents the Lindhard model, while the blue (back) filled histogram represents the Sorensen model. In the Sorensen model, many points are pushed to zero due to the presence of a cutoff energy, leading to a peak in the first bin that is not present in the Lindhard model. For both models, we use $k = 0.178$ and $q = 0.00075$. The solid-line unfilled histogram represents the Lindhard model with a 5× better resolution, and the dashed unfilled histogram represents the Sorensen model with that resolution. Both of these show much taller, narrower peaks than their counterparts.

different angular distributions—although the total cross sections are close—and could affect our simulation. The difference is unlikely to change our results, because the γ environment is dominated by capture γ's from the surrounding materials and across a wide range of energies (1–10 MeV). That spectrum cannot create features similar to capture-induced NRs.

Direct neutron scatters (single or multiple) are also not likely to change our results. Hi-precision neutron physics NeutronHP is included in our GEANT4 physics list. While the modeling is not likely to be perfect, our direct-scatter neutron environment has a wide range of energies—from below 1 MeV to as high as around 9 MeV with no strong energy features. This neutron spectrum will create a nearly featureless quasiexponential background with very little impact from multiple scatters [45].

Recently, there has been interest in inelastic processes that can occur at these energies, namely, the Migdal effect and atomic bremsstrahlung [46–48]. We did not model these backgrounds, because a calculation showed that they would be 2%–4% of the expected capture signal.

VI. FITTING

Our data analysis consists of fitting a simulated PuBe spectrum to background-subtracted data. The simulated spectrum consists of both thermal neutron-capture events as well as PuBe-generated noncapture ERs and NRs. Data from the background dataset are normalized and subtracted from the PuBe signal data before being compared to simulation. We accounted for the data-taking and cut efficiencies by applying the relevant corrections to the data after the cuts.

A. Integral method

Our preferred method of constraining the ionization yield is to fit a well-motivated theoretical model with a small number of parameters to the data. However, the ionization yield as a function of energy has been shown to be a poorly understood theoretical construct [9,10,17]. Our approach to deal with this situation was to use an "integral method" similar to Chavarria [9] while assuming consistency with the higher-energy Izraelevitch data [8]. We did this with and without the inclusion of the neutron-capture-induced NRs to give a generic understanding of the plausibility of the ionization functions in each situation. Note that the integral method can reproduce given experimental data with *any* NR component, since it essentially has infinitely many degrees of freedom. This procedure was developed in detail by Mast [32].

Executing the procedure assuming that neutron-capture-induced NRs were *not* present produced an oddly shaped yield curve with an anomalous increase below 1 keV recoil energy (see Fig. 6). Conversely, including the neutron-capture-induced NRs (not shown) gave a yield curve that was better behaved at low energies and more consistent with previous measurements, especially those of the DAMIC Collaboration [9].

The results were calculated with the assumption that the Fano factor for NRs, $F_{\mathrm{NR}} = 0.1161$, is the same as for ERs. Repeating this exercise with different values showed almost no change in the resulting yield band for $F_{\mathrm{NR}} < 5$. This is not surprising, because, even at a low NR Fano factor, the features in the capture spectrum are smeared.

B. Markov chain Monte Carlo (MCMC) method

A direct fit to the data was also performed, including different parametrized yield models. As mentioned above, no ionization yield model in the literature seems fully appropriate for NRs at these low recoil energies, but performing the fit allowed us to compare our data using well-established statistical techniques and ionization yield models with a limited number of parameters. We avoided optimizing our fits to an arbitrary functional form without convincing theoretical motivation. Nonetheless, our results imply (i) a clear identification of the neutron-capture-induced NR signal; (ii) a further indication that the long-popular Lindhard model [7] is not a complete description; and (iii) a preference for a yield model which goes to near-zero ionization yield at a finite recoil energy—a possibility with far-reaching implications for DM or CEνNS science.

The fitting was accomplished using the MCMC ensemble sampler EMCEE [49]. Our method follows closely the method of Scholz [10] and was developed by Mast [32]. The fit was performed with the following yield models [$Y(E_r)$]: Lindhard [7], Sorensen [11], Chavarria [9], and adiabatic correction (AC) [50]. Independent scaling factors for each of the three simulated spectra—capture, ER, and noncapture NR—were included as fit parameters. The Fano factor for NRs was also allowed to float in the fits. To obtain the posterior distributions via the MCMC technique, a flat prior distribution in reasonable parameter ranges was assumed.

To accommodate the asymmetric uncertainties which resulted from our cuts and background subtraction methodology, we described the observed counts in each bin with a split-normal [51] distribution with upper and lower uncertainties σ_{hi} and σ_{low}, respectively. The log-likelihood function is

$$\ln(\mathcal{L}_{S\mathrm{Norm}}(\vec{c};\vec{\mu},\vec{\sigma}_{\mathrm{low}},\vec{\sigma}_{\mathrm{hi}})) = \sum_i \left[\frac{1}{2}\ln\left(\frac{2}{\pi}\right) - \ln(\sigma_{\mathrm{low},i}+\sigma_{\mathrm{hi},i}) - \frac{1}{2}\left(\frac{c_i-\mu_i}{\sigma_i}\right)^2\right], \tag{2}$$

where $\vec{c}$—which implicitly depends on all the fit parameters—is the set of simulated counts, $\vec{\mu}$ are the average measured rates for each bin, $\vec{\sigma}_{\mathrm{hi}}(\vec{\sigma}_{\mathrm{low}})$ is the width parameter for points above (below) μ, and σ_i is a piecewise

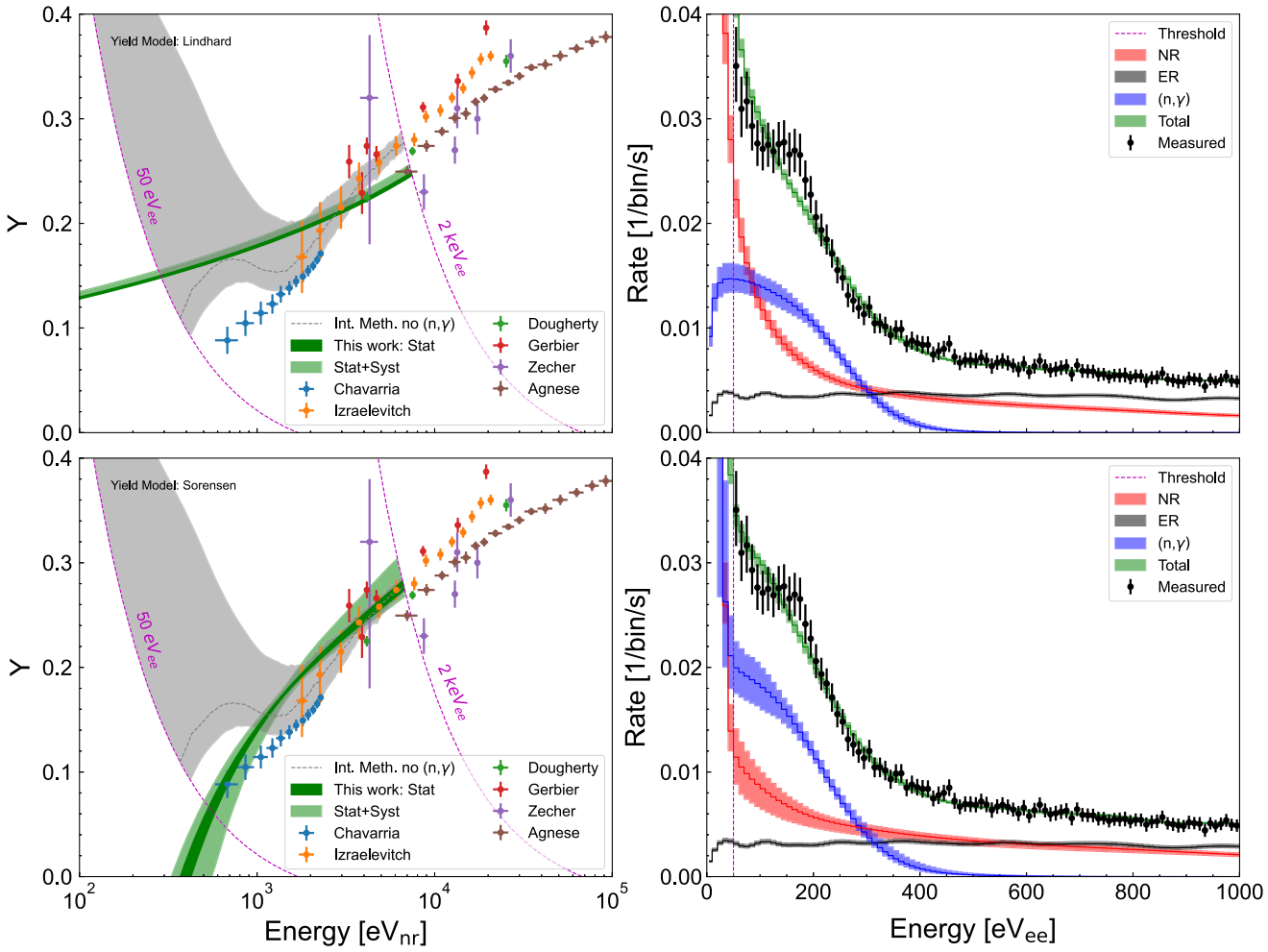

FIG. 6. MCMC fitting results for Lindhard (top) and Sorensen (bottom) yield models. Left: Best-fit yield curves using the specified yield model are shown with statistical and systematic errors, in comparison with multiple published measurements. The detector threshold level is shown as the low magenta dashed curve. Right: range of best-fit background-subtracted reconstructed spectra. Shaded bands represent the 1-sigma equivalent range of rates in each energy bin. On each of the left-hand plots, the result of the integral method *without* including the neutron-capture-induced NRs is shown (gray dashed lines and gray bands); the resulting ionization yield function is poorly constrained and oddly shaped, implying the necessity of the neutron-capture-induced NR contribution.

function giving the upper width if c_i is above μ_i and the lower width otherwise.

The maximum likelihood goodness of fits are shown in Table II. While the Sorensen model yields the best fit by far, even that fit is not particularly good. The table also shows the goodness of fits for a parallel fit that does *not* include the neutron-capture component. In all cases, there is a strong preference for the inclusion of the neutron-capture component (at least $\sim 25\sigma$). Using a likelihood ratio test [52,53], there is a preference to reject the Lindhard model in favor of any other with a p value of at most 4.4×10^{-13}. The best-fit values of the scaling factors of the simulated spectra indicate that the absolute rates predicted by the GEANT4 simulation do not agree with the observed data.

TABLE II. Table of best-fit χ^2/d.o.f. values for several yield models. Calculated using only statistical uncertainties.

Model	χ^2/d.o.f.	χ^2/d.o.f. (no cap.)	Par.
Lindhard	$722.8/190 = 3.804$	$1653.7/191 = 8.659$	k
Sorensen	$306.7/189 = 1.623$	$1765.7/190 = 9.293$	k, q
Chavarria	$670.4/189 = 3.547$	$2010.3/190 = 10.581$	k, a
AC	$525.0/189 = 2.778$	$1808.4/190 = 9.518$	k, ξ

C. MCMC results

The models we believe deserve the most focus are the Lindhard model for historical significance and the Sorensen model because of its yield falloff at low energies. The Sorensen model is characterized by $Y_{\mathrm{Sor}}(E_r, k, q) = Y_{\mathrm{L}}(E_r, k) - q/\varepsilon(E_r)$, where Y_{L} is the Lindhard model and $\varepsilon(E_r)$ is the unitless version of E_r used in the Lindhard model. The Sorensen model was the best-fitting

model, and the parameters were $k = 0.151^{+040}_{-0.007}$ and $q = 1.96^{+1.32}_{-0.54} \times 10^{-3}$. Figure 6 shows the details of the fit results.

VII. CONCLUSIONS

This experiment studied nuclear recoils in silicon down to 450 eV and analyzed the spectrum to find evidence for induced NR via neutron capture. The final measured spectrum strongly prefers a thermal neutron-capture-induced NR component, a preference that corresponds to 25σ or more for each ionization model studied. If the (n, γ) process is *not* included, the resulting shape of the ionization yield function $Y(E_r)$ becomes unusually distorted to make up for it, as demonstrated by the integral method.

Our results favor the Sorensen ionization yield model (which has a low-energy ionization cutoff) to the standard Lindhard model, giving a p value of the likelihood ratio test [53] of less than 4.4×10^{-13}. While it is clear that a "perfect" fit to the data is possible for *some* ionization yield model $Y(E_r)$, none of the proposed models fit well. The perfect fit that would be given by the integral method with (n, γ) included provides little understanding of the process and, in particular, how it may depend on field strength and/or temperature, so it was omitted. More theoretical work on this process is required first.

Neutron-capture-induced events provide an excellent window into very low-energy NRs. Further studies on NR ionization yield in silicon are necessary to establish the behavior at low energies and to quantify a possible 100-eV-scale yield threshold. Improvements are planned for the next experiment. The recoil energy threshold can be lowered by better background mitigation and improved detector resolution. Tagging the gammas emitted after capture will be a significant improvement in the experimental technique, since the capture spectrum can then be isolated.

The data that support the findings of this study are openly available via the Open Science Framework (OSF) [54].

ACKNOWLEDGMENTS

The authors thank the SuperCDMS Collaboration for the use of the detector and readout electronics. This work was supported by Department of Energy Grants No. DE-SC0012294 and No. DE-SC0021364 and Grant No. NSF-1743790 via the Partnerships for International Research and Education programs (PIRE). We also acknowledge the support of the Germanium Materials and Detectors Advancement Research Consortium (GEMADARC).

[1] O. Abramoff *et al.* (SENSEI Collaboration), Phys. Rev. Lett. **122**, 161801 (2019).
[2] D. W. Amaral *et al.*, Phys. Rev. D **102**, 091101 (2020).
[3] I. Alkhatib *et al.* (SuperCDMS Collaboration), Phys. Rev. Lett. **127**, 061801 (2021).
[4] E. Aprile *et al.* (XENON Collaboration), Phys. Rev. Lett. **123**, 251801 (2019).
[5] A. H. Abdelhameed *et al.* (CRESST Collaboration), Phys. Rev. D **100**, 102002 (2019).
[6] D. S. Akerib *et al.* (LUX Collaboration), Phys. Rev. D **101**, 042001 (2020).
[7] J. Lindhard, V. Nielsen, M. Scharff, and P. Thomsen, Kgl. Danske Videnskab., Selskab. Mat. Fys. Medd. **33**, 10 (1963).
[8] F. Izraelevitch *et al.*, J. Instrum. **12**, P06014 (2017).
[9] A. E. Chavarria *et al.*, Phys. Rev. D **94**, 082007 (2016).
[10] B. J. Scholz, A. E. Chavarria, J. I. Collar, P. Privitera, and A. E. Robinson, Phys. Rev. D **94**, 122003 (2016).
[11] P. Sorensen, Phys. Rev. D **91**, 083509 (2015).
[12] G. Gerbier *et al.*, Phys. Rev. D **42**, 3211 (1990).
[13] B. L. Dougherty, Phys. Rev. A **45**, 2104 (1992).
[14] The first reference here is the Lindhard model of the 1960s, and the rest of the papers are experimental studies spanning almost three decades and beginning almost 30 years after the Lindhard model's publication, yet they all make exclusive use of that model and mention it *in the abstract or introduction* despite it being known to be flawed for low energies.
[15] L. Thulliez *et al.*, J. Instrum. **16**, P07032 (2021).
[16] K. W. Jones and H. W. Kraner, Phys. Rev. A **11**, 1347 (1975).
[17] J. I. Collar, A. R. L. Kavner, and C. M. Lewis, Phys. Rev. D **103**, 122003 (2021).
[18] R. Agnese *et al.* (SuperCDMS Collaboration), Phys. Rev. D **95**, 082002 (2017).
[19] D. Akerib *et al.*, Nucl. Instrum. Methods Phys. Res., Sect. A **591**, 476 (2008).
[20] K. D. Irwin, S. W. Nam, B. Cabrera, B. Chugg, and B. A. Young, Rev. Sci. Instrum. **66**, 5322 (1995).
[21] Oxford Instruments, Tubney Woods, Abingdon, Oxfordshire OX13 5QX, United Kingdom.
[22] R. Agnese *et al.* (SuperCDMS Collaboration), Phys. Rev. Lett. **112**, 041302 (2014).
[23] S. Hansen, F. DeJongh, J. Hall, B. A. Hines, M. E. Huber, T. Kiper, V. Mandic, W. Rau, T. Saab, D. Seitz, and K. Sundqvist, in *Proceedings of the IEEE Nuclear Science Symposuim Medical Imaging Conference* (IEEE, New York, 2010), pp. 1392–1395.
[24] P. N. Luke, J. Appl. Phys. **64**, 6858 (1988).
[25] B. S. Neganov and V. N. Trofimov, Otkryt. Izobret. **146**, 215 (1985).
[26] R. Pehl, F. Goulding, D. Landis, and M. Lenzlinger, Nucl. Instrum. Methods **59**, 45 (1968).
[27] L. Stewart, Phys. Rev. **98**, 740 (1955).

[28] S. Golwala, Exclusion limits on WIMP-nucleon elastic scattering cross-section from the cryogenic dark matter search, Ph. D. thesis, University of California, Berkeley, 2000.
[29] F. R. O'Donnell, E. L. Etnier, G. A. Holton, and C. C. Travis, Oak Ridge National Laboratory Technical Report, 10.2172/5999867.
[30] U. Fano, Phys. Rev. **72**, 26 (1947).
[31] B. Lowe, Nucl. Instrum. Methods Phys. Res., Sect. A **399**, 354 (1997).
[32] N. Mast, Cryogenic detector development for superCDMS, Ph.D. Thesis, University of Minnesota, 2020.
[33] R. Clarke, An athermal phonon mediated dark matter detector with surface event discrimination, Ph.D. thesis, Stanford University, 2003.
[34] A. Villano, K. Harris, and S. Brown, J. Open Source Software **7**, 3993 (2022).
[35] K. J. R. Rosman and P. D. P. Taylor, Pure Appl. Chem. **70**, 217 (1998).
[36] K. SHIBATA *et al.*, J. Nucl. Sci. Technol. **48**, 1 (2011).
[37] S. Raman, E. T. Jurney, J. W. Starner, and J. E. Lynn, Phys. Rev. C **46**, 972 (1992).
[38] V. F. Weisskopf, Phys. Rev. **83**, 1073 (1951).
[39] J. Allison *et al.*, IEEE Trans. Nucl. Sci. **53**, 270 (2006).
[40] S. Agostinelli *et al.*, Nucl. Instrum. Methods Phys. Res., Sect. A **506**, 250 (2003).
[41] J. Brown, M. Dimmock, J. Gillam, and D. Paganin, Nucl. Instrum. Methods Phys. Res., Sect. B **338**, 77 (2014).
[42] L. Thulliez, C. Jouanne, and E. Dumonteil, Nucl. Instrum. Methods Phys. Res., Sect. A **1027**, 166187 (2022).
[43] M. Omer and R. Hajima, Nucl. Instrum. Methods Phys. Res., Sect. B **405**, 43 (2017).
[44] D. E. Cullen, J. H. Hubbell, and L. Kissel, Technical Report No. UCRL-50400-Vol.6-Rev.5, 1997, https://www.osti.gov/biblio/295438.
[45] M. F. Albakry *et al.* (SuperCDMS Collaboration), arXiv:2202.07043.
[46] M. Ibe, W. Nakano, Y. Shoji, and K. Suzuki, J. High Energy Phys. 03 (2018) 194.
[47] M. J. Dolan, F. Kahlhoefer, and C. McCabe, Phys. Rev. Lett. **121**, 101801 (2018).
[48] C. Kouvaris and J. Pradler, Phys. Rev. Lett. **118**, 031803 (2017).
[49] D. Foreman-Mackey, D. W. Hogg, D. Lang, and J. Goodman, Publ. Astron. Soc. Pac. **125**, 306 (2013).
[50] D. J. Ficenec, S. P. Ahlen, A. A. Marin, J. A. Musser, and G. Tarlé, Phys. Rev. D **36**, 311 (1987).
[51] K. F. Wallis, Stat. Sci. **29**, 106 (2014).
[52] S. S. Wilks, Ann. Math. Stat. **9**, 60 (1938).
[53] R. Agnese *et al.* (SuperCDMS Collaboration), Phys. Rev. D **99**, 062001 (2019).
[54] K. Harris, A. N. Villano, and M. Fritts, First observation of isolated nuclear recoils following neutron capture, 10.17605/OSF.IO/G4ENQ.